# SUPPLEMENTARY MATERIAL of "Ambient-dependent reversal of unidirectional light scattering by metal-dielectric hybrid plasmonic nanoantenna"

Shuto Watanabe, Ryuichi Ohta*, Tsukasa Katayama, Yoshito Tanaka*

**Design of the plasmonic nanoantennas**

We designed the geometries of the gold nanorods and the dielectric shield to invert the relative phase of the scattered light when the surroundings medium changes from air (n=1.00) to water (n=1.33). Since water redshifts the resonance wavelength of unshielded nanorods, the initial resonance of the unshielded nanorod must be shorter than that of the shielded one. The dielectric shield increases the intrinsic plasmonic resonance wavelength in air while it reduces the influence of the surrounding refractive index. We optimized the lengths, widths, thicknesses of each gold nanorod and the $Al_2O_3$ dielectric shield through numerical calculations based on finite element method (COMSOL Multiphysics). Figure S1 shows the calculated scattering intensities of the individual gold nanorods under various ambient refractive indices using the geometries described in the main text. The resonance of the unshielded nanorod shifts from 755 to 840 nm as the refractive index increases, whereas the resonance of the shielded nanorod remains fixed near 800 nm. These parameters confirm that relative phase inversion can be achieved with appropriate geometric design and refractive index contrast.

We then investigated the separation distance between the two nanorods to determine the geometric retardation that maximizes directional scattering both in air and water. As described in Ref. 7, directionality is maximized when the detuning between the two resonances equals the individual resonance linewidths. Under this condition, the optimal distance corresponds to a quarter of the nanoantenna array period in the x-direction, equivalent to a retardation of $\pi/2$ at the diffraction angle. However, to reverse the direction of the scattered light, the detuning between shielded and unshielded nanorods tends to be smaller than the linewidths, because the amount of the resonance shift of unshielded nanorods is limited with practical solvents. For example, in our optimized design for air and water, the detuning is about 50 nm while the linewidth is about 130 nm as shown in Figure S1. Consequently, the relative phase of the two plasmonic nanorods does not reach $\pi/2$. To compensate, the geometric retardation was designed to exceed $\pi/2$, ensuring that the sum of the plasmonic phase difference and geometric retardation is equal to $\pi$. Figure S2a presents analytically calculated directionalities as functions of the phases due to the plasmonic resonances ($\phi_p$) and geometric distances ($\phi_d$) using following equation.

$$log_{10}\left(\left|\frac{\cos\left((\phi_d-\phi_p)/2\right)}{\cos\left((\phi_d+\phi_p)/2\right)}\right|^2\right)$$

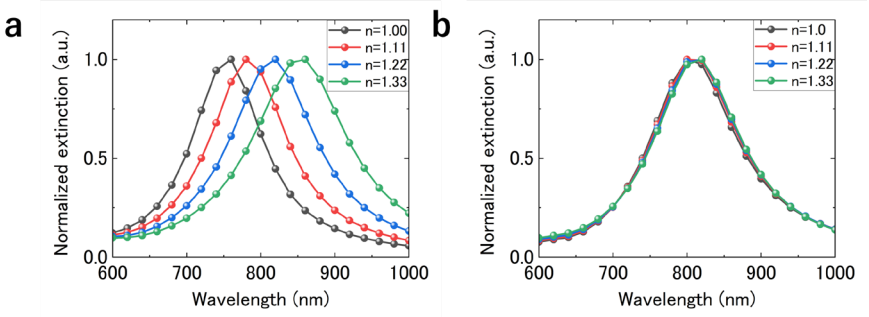


**Figure S1.** Numerically calculated scattering spectra of the nanoantenna under various surrounding refractive indexes without dielectric shield (a) and with the shield (b).

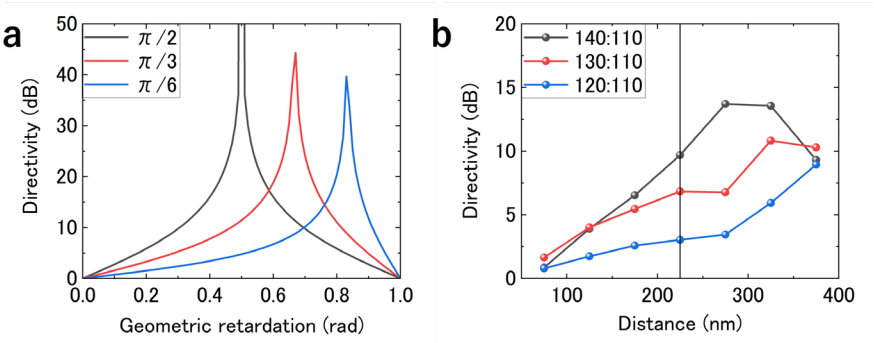


**Figure S2.** (a) Calculated directivity depending on geometric retardation. Inset shows the relative phases of plasmonic resonances. (b) Measured directivity with various lengths and distances of the nanorods. Inset shows the lengths of the paired nanorods, where larger length difference makes higher relative phases.

As the relative phase of plasmonic resonances decreases, a larger geometric retardation is required to maintain high directionality. To validate this design strategy, we fabricated unshielded paired nanorods with varying length combinations and distances. Here, larger difference in the length makes higher relative phase coming from plasmonic resonances, while larger distance provides larger geometric retardations. The measured directionalities in air as shown in Figure S2b were consistent with the analytical calculation based on our design strategy. In practical, the relative phase of the plasmonic resonances cannot be fully controlled. Based on this analysis, we selected a nanorod spacing of 350 nm, which provides a geometric retardation of 0.78π for a periodicity of 900 nm.

### Fabrication of the plasmonic nanoantennas

Plasmonic antennas were fabricated through the following steps. A positive electron-beam resist film was spin-coated onto a glass substrate to a thickness of 170 nm. The nanorod pattern was defined by electron beam lithography (EBL) at an accelerating voltage of 130 kV, followed by development. A 5-nm-thick chromium (Cr) adhesion layer and a 50-nm-thick gold layer were then deposited by sputtering. The resist was lifted off, leaving gold nanorods on the substrate. The Cr layer might broaden the linewidth in the extinction spectrum, as shown in Fig. S3a. The linewidth broadening decreases the relative phase between the two nanorods, which might reduce the controllability of the unidirectional light scattering. Although the decrease of the relative phase can be compensated with the geometric retardation, thinner Cr or other adhesion layer with low optical absorption will improve the controllability of the directivity with respect to the surrounding refractive index. Figure S3b shows the SEM image without dielectric shield. We extracted the length and width of each nanorod from the image. Next, the pattern for the $Al_2O_3$ dielectric shields was defined using an EBL overlay process aligned by pre-fabricated alignment marks, followed by development. A 70-nm-thick $Al_2O_3$ layer was deposited via pulsed laser deposition. The resist mask was removed, and the dielectric shields remained selectively on top of the nanorods, as shown in Fig. 2.

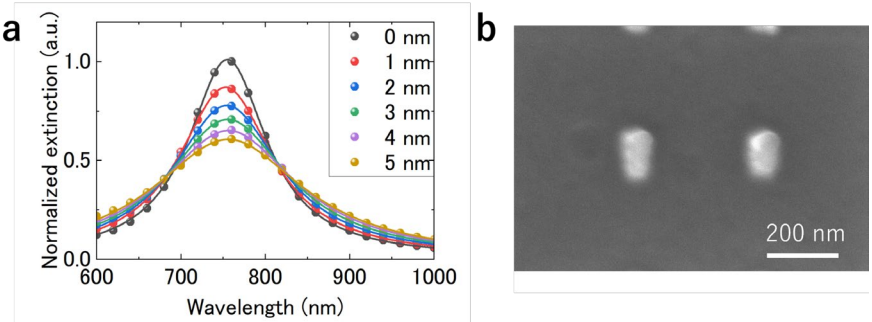


**Figure S3.** (a) Numerically calculated normalized extinction spectra with Cr adhesion layer. Inset shows the thickness of Cr. (b) SEM image of the nanoantennas without the dielectric shield.

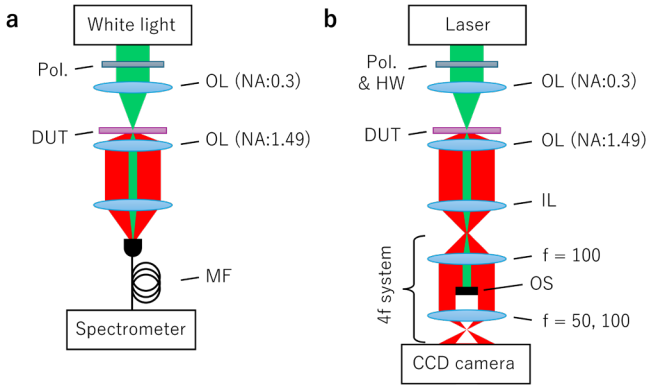


**Figure S4.** Schematic images of experimental setups for spectroscopy (a) and Fourier imaging measurements (b)

### Experimental setups

Figure S4a illustrates the schematic of the experimental setup for spectroscopic measurements. The samples (DUT: device under test) were mounted on an inverted microscope (Nikon Ti-U). Linearly polarized white light, controlled by a polarizer (Pol.), was focused onto the DUT through an objective lens (OL) with a numerical aperture (NA) of 0.3, illuminating an area of approximately 80 μm$^2$. The transmitted light, which included both the incident light and that scattered by the nanoantennas, was collected using another objective lens (NA = 1.49). This light was coupled into a multimode fiber (MF, 100 μm core diameter) via a fiber collimator, and the extinction spectra were recorded using a fiber-coupled spectrometer. The extinction spectra of the samples were obtained by calculating $A(\lambda) = \left(T_{Ref}(\lambda) - T_{DUT}(\lambda)\right)/T_{Ref}(\lambda)$ , in which $T_{DUT}$ and $T_{Ref}$ are the intensities of the transmitted light with and without the samples, respectively.

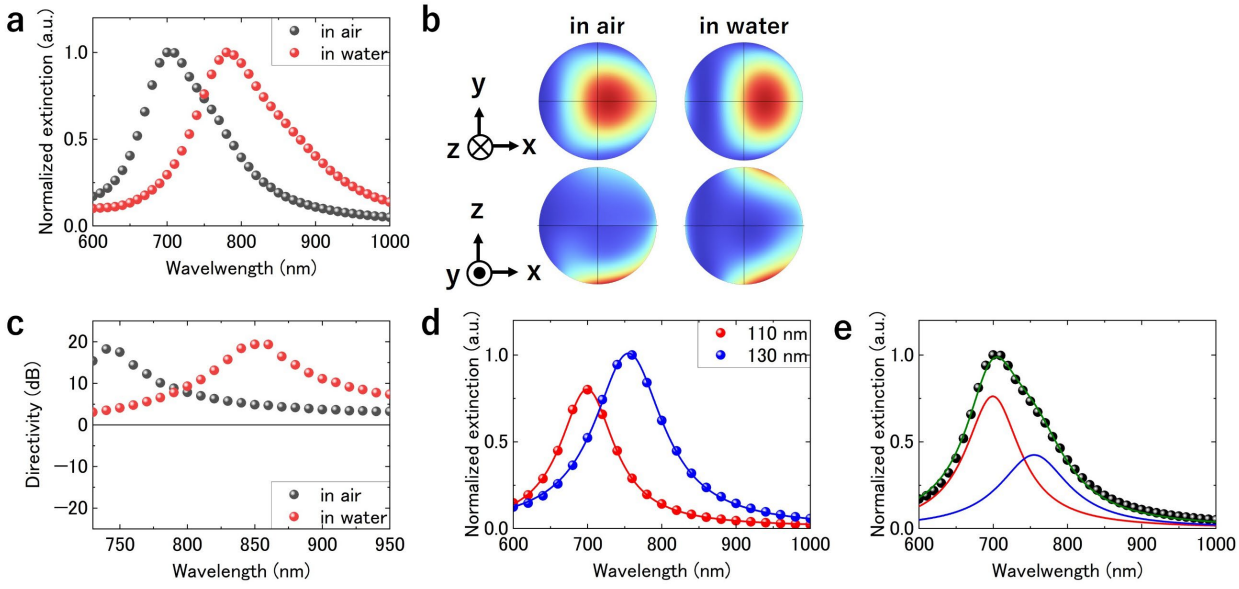


**Figure S5.** Numerical calculations of the non-shielded nanoantenna with and without water droplet. (a) Extinction spectra. (b) Scattering intensity distributions in the x-z plane. Blue dashed lines indicate the refracted directions. (c) Wavelength dependences of directivity. (d) Extinction spectra of individual nanorods with lengths of 130 nm and 110 nm without a water droplet. (e) Extinction spectrum of the non-shielded nanoantenna fitted with the spectra of single nanorods with lengths of 110 nm (red curve) and 130 nm (blue curve), respectively.

Figure S4b shows the schematic of the Fourier imaging setup. Linearly polarized light from a Ti:sapphire laser was adjusted using a polarizer and a half-wave plate (HW). The laser beam was focused on the DUT and collected using the same objective lenses. The back focal plane (BFP) inside the microscope was imaged onto a CCD camera through an imaging lens (IL) and a 4f optical system. An opaque stopper (OS) placed in the Fourier plane blocked the incident laser beam. This Fourier imaging configuration could be easily switched to a dark-field imaging setup by replacing the lens in front of the CCD from one with $f$ = 50 mm to $f$ = 100 mm.

**Numerical analyses of the non-shielded nanoantenna**

Figures S5 show the extinction spectra, spatial distribution of the scattered light intensity, wavelength dependence of the directivity for the non-shielded nanoantenna with and without water droplet. In contrast to Figure 4a, the extinction spectrum exhibits a redshift while maintaining its linewidth. It indicates the separation of the resonance frequencies of the two nanorods and the relative phase of scattered light do not significantly change. Therefore, the light scattering direction is not reversed by changing the ambient medium. These numerical analyses agree with the experimental results shown in Figure 3a, 3c, and 3e.

Figure S5d shows the extinction spectra of individua nanorods with lengths of 130 nm and 110 nm without water droplets. Larger dipole moment of the 130-nm nanorod makes the peak intensity higher than that of the 110-nm nanorod. Figure S5e shows the spectral decomposition of the non-shielded nanoantenna with two peaks associated with the individual resonances of the 130-nm and 110-nm nanorods. The plasmonic coupling between the two nanorods modifies their intensity ratio, which makes the spectrum of the nanoantenna appear as a single peak. The agreement between these calculated spectra supports the interpretation of the spectral features and decomposition of Fig. 3a.

**Near-field distribution and leakage ratio of the field**

Figure S6a shows the near-field distributions ($\sqrt{{E_x}^2 + {E_y}^2 + {E_z}^2}$) with and without the 150-nm-width shield in X-Y plane at the top and bottom of the nanoantenna. To discuss the influence of the shield geometry on unidirectional light scattering, we numerically evaluated leakage ratio of the near field from the shielded region, defined as the field amplitude outside the shield divided by the total field amplitude, as shown in Fig. S6b. The leakage ratio is about 98% for the 150-nm-wide shield used in the experiments and reaches almost 100% for the 200-nm-wide shield. The leakage of the near field makes the resonance of the shielded nanorod sensitive to the surrounding refractive index. The small resonant wavelength shift of the shielded nanorod shown in Fig. S1b might be attributed to the field leakage. The electric field changes discontinuously at the boundary of the shield owing to the refractive index difference. This discontinuous field distribution affects the interference of the scattered light in air and water regions. However, the lateral scattering in forward direction is not influenced, since the scattered light propagates through the grass substrate.

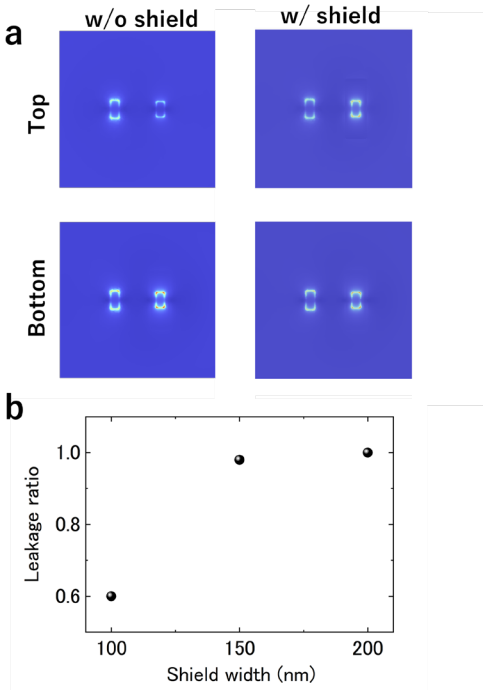


**Figure S6.** (a) Numerical calculated near-field distribution with and without dielectric shield in X-Y plane at the top and bottom of the antenna. (b) The leakage ratio as a function of the shield width.